ADVANCED MATERIALS
www.advmat.de

Passivation of the Buried Interface via Preferential Crystallization of 2D Perovskite on Metal Oxide Transport Layers

*Bin Chen, Hao Chen, Yi Hou, Jian Xu, Sam Teale, Koen Bertens, Haijie Chen, Andrew Proppe, Qilin Zhou, Danni Yu, Kaimin Xu, Maral Vafaie, Yuan Liu, Yitong Dong, Eui Hyuk Jung, Chao Zheng, Tong Zhu, Zhijun Ning, and Edward H. Sargent**

The open-circuit voltage (V_{oc}) of perovskite solar cells is limited by non-radiative recombination at perovskite/carrier transport layer (CTL) interfaces. 2D perovskite post-treatments offer a means to passivate the top interface; whereas, accessing and passivating the buried interface underneath the perovskite film requires new material synthesis strategies. It is posited that perovskite ink containing species that bind strongly to substrates can spontaneously form a passivating layer with the bottom CTL. The concept using organic spacer cations with rich $-NH_2$ groups is implemented, where readily available hydrogens have large binding affinity to under-coordinated oxygens on the metal oxide substrate surface, inducing preferential crystallization of a thin 2D layer at the buried interface. The passivation effect of this 2D layer is examined using steady-state and time-resolved photoluminescence spectroscopy: the 2D interlayer suppresses non-radiative recombination at the buried perovskite/CTL interface, leading to a 72% reduction in surface recombination velocity. This strategy enables a 65 mV increase in V_{oc} for NiO_x based p–i–n devices, and a 100 mV increase in V_{oc} for SnO_2-based n–i–p devices. Inverted solar cells with 20.1% power conversion efficiency (PCE) for 1.70 eV and 22.9% PCE for 1.55 eV bandgap perovskites are demonstrated.

1. Introduction

Low cost and facile fabrication have enabled rapid increases in the power conversion efficiency (PCE) in single-junction metal halide perovskite solar cells (PSCs).[1,2] Further advances in PCE of PSCs will rely on the improvement of open-circuit voltage (V_{oc}) and fill factor (FF), as the short circuit current (J_{sc}) is almost at its Shockley–Queisser (SQ) limit.[3–5] In addition, multi-junction perovskite cells, which promise to break the single-junction SQ limit, require an efficient wide-bandgap top cell that can sustain a high voltage output.[6,7]

V_{oc} is determined by the dark recombination current density, related to the non-radiative recombination of carriers in real devices.[8] With sufficient carrier diffusion lengths in perovskite bulk,[9] non-radiative recombination takes place primarily at the carrier transport layer (CTL) and perovskite interface.[4,10,11] High surface trap states at these heterointerfaces, therefore, contribute to V_{oc} loss. For instance, though NiO_x has been demonstrated to be a stable inorganic replacement for organic hole-transport layers (HTL), the V_{oc} values in these devices are lower than that in their organic counterparts.[12–14] The inorganic CTL/perovskite interface is prone to defects that function as non-radiative recombination centers[15–17] or as extraction barriers.[18]

The top perovskite/carrier transport layer interface has been modified by post-treatment to boost V_{oc}.[3,19,20] Organic species including Lewis acids–bases[21–23] and large cations,[3,20,24,25] thin inorganic layers, such as LiF,[10] Al_2O_3,[26] and lead oxysalts[27] improve the perovskite/CTL contact. A 2D/3D hybrid structure facilitates carrier extraction[28–30] and increases open-circuit voltage.[31–34] In contrast, passivation is less established at the buried interface between the perovskite and CTL. Treating the substrate surface prior to perovskite deposition is a widely practiced strategy. Graphene,[35,36] perovskite,[31,37,38] and quantum dot[39] interlayers, along with amorphous metal oxide coatings,[40] are used to enhance band alignment; while organic molecules and polymers suppress interfacial non-radiative recombination.[24,41–43] However, this introduces additional fabrication steps, and the passivating layer can be washed away in subsequent spin-coating processes. Although excessive PbI_2 introduced to the buried interface via stoichiometric control provides an intrinsic route to improve the interface,[44] unreacted PbI_2 negatively impacts device operation stability.[45] It is therefore of interest to find a more effective means to passivate the buried interface.

B. Chen, H. Chen, Y. Hou, J. Xu, S. Teale, K. Bertens, H. Chen, A. Proppe, M. Vafaie, Y. Liu, Y. Dong, E. H. Jung, C. Zheng, T. Zhu, E. H. Sargent
Department of Electrical and Computer Engineering
University of Toronto
35 St George Street, Toronto, Ontario M5S 1A4, Canada
E-mail: ted.sargent@utoronto.ca

H. Chen, Q. Zhou, D. Yu, K. Xu, Z. Ning
School of Physical Science and Technology
ShanghaiTech University
Shanghai 201210, China

The ORCID identification number(s) for the author(s) of this article can be found under https://doi.org/10.1002/adma.202103394.

DOI: 10.1002/adma.202103394

In this work, we sought to use perovskite precursors mixed with large organic cations for the spontaneous formation of a 2D passivation layer at the buried interface. A comparison between different spacer cations including n-butylammonium (BA), ethylammonium (EA), dimethylammonium (DMA), and guanidinium (GUA) reveals that large binding affinity of cations to substrates plays a key role in the successful implementation of the concept. We find that EA and DMA are not able to form a 2D phase while the 2D BA phase does not form at the perovskite/CTL interface. Only a GUA-containing precursor forms a 2D GUA_2PbI_4 phase at the buried interface, which is attributed to its symmetric structure and abundance of $-NH_2$ groups. The preferential crystallization of GUA_2PbI_4 at the bottom interface is induced by the NiO_x substrate: readily available hydrogens from amino groups in GUA bind strongly to undercoordinated oxygens in the NiO_x, serving as nuclei for GUA_2PbI_4 growth. This interaction passivates the otherwise Ni deficient NiO_x surface.[12] As a result, the formation of 2D GUA_2PbI_4 suppresses non-radiative recombination at the perovskite/NiO_x interface, leading to a 65 mV enhancement of V_{oc}. We demonstrate a V_{oc} of 1.23 V, the highest among inverted devices using NiO_x as HTL; and a PCE of 20.1% using a perovskite-silicon tandem compatible 1.70 eV bandgap perovskite. Furthermore, the same strategy applied to 1.55 eV bandgap perovskite yields a champion PCE of 22.9%.

2. Results and Discussion

Here we used a previously reported 1.70 eV dimethylammonium-formamidinium-cesium (CsFADMA) triple cation perovskite composition as a baseline (control).[46] Its bandgap value is particularly attractive for perovskite/silicon tandem solar cell applications.[7] For precursors mixed with different cations, we replaced DMA with an equal molar ratio of EA, BA, and GUA. X-ray diffraction (XRD) patterns (**Figure 1**A) show no low dimensional phase formation in EA- and DMA-containing films, which is likely due to their relatively small cation size. On the contrary, 2D perovskite phases are clearly present in both BA and GUA films. Two peaks at 9° and 13.5° from BA films agree with the simulated pattern of the 2D $BA_2MAPb_2I_7$ phase (MA = methylammonium).[47] Since no MA was used to fabricate these films, we conclude that the 2D phase in BA films is $BA_2FA_xCs_{(1-x)}Pb_2I_7$.[48] Emerging peaks at 11.6° and 13.05° in GUA films can be indexed into the 2D GUA_2PbI_4 phase.[49,50] NiO_x is reported to react with perovskite precursors producing $PbI_{2-x}Br_x$, which acts as a hole extraction barrier, significantly limiting V_{oc}.[18] In contrast, we note that none of our samples deposited on NiO_x substrates exhibit detectable $PbI_{2-x}Br_x$ at 12.7°, suggesting that our NiO_x/perovskite interface is qualitatively different from the recent work. Differences in NiO_x synthetic procedures and different perovskite precursor compositions may account for this difference.

We then sought to understand whether the 2D phases are present on interfaces and probed using a combination of absorptance and reflectance spectroscopy. We reasoned that if there is a 2D interlayer on either the top or bottom perovskite surface, the optical response of the perovskite film would be perturbed by the added dielectric function of the 2D phase. To obtain accurate absorption spectra, samples were mounted in an integrating sphere. Monochromated light was incident on one side of the film stack (glass/CTL/perovskite). The reflectance and absorptance spectra of BA and GUA films were subtracted from those of the control to yield differential reflectance and absorptance spectra.

Glass-incident differential absorptance spectra of GUA films show a drop at ≈455 nm (Figure 1B). It is clear from the differential reflectance spectra that the reduced blue absorption is caused by increased reflectance at the same wavelength. While perovskite bulk absorbs strongly in 400–500 nm region, reflection is an interface phenomenon caused by the refractive index mismatch of layers in a dielectric film stack. As a result, interface reflection occurs before bulk absorption and changes in reflectance indicate modifications at the interface. Considering the absorption peak of a GUA_2PbI_4 thin film at ≈455 nm (Figure S1A, Supporting Information), the reflectance increase is caused by a strong dielectric function modulation around the absorption wavelength,[51,52] confirmed by a ≈30% variation of

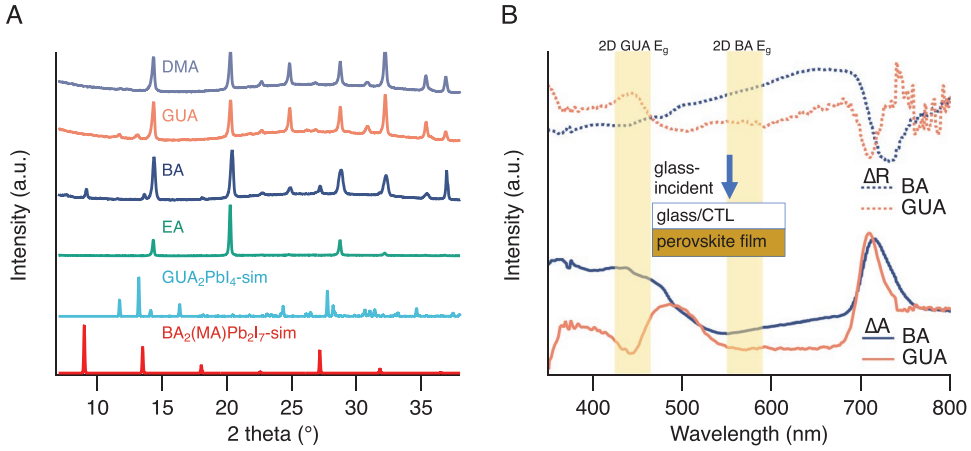

Figure 1. Formation of 2D perovskite phases with different organic cations. A) XRD patterns of DMA-, GUA-, BA-, EA-containing films deposited on NiO_x substrate and simulated patterns for GUA_2PbI_4 and $BA_2MAPb_2I_7$. B) Glass-incident differential absorptance and reflectance spectra of BA and GUA films.

refractive indexes measured by ellipsometry (Figure S1B, Supporting Information). On the contrary, we observe no particular feature around the bandgap of the 2D BA phase at ≈580 nm,[54] despite a sharp change in its refractive index.[53] We, therefore, conclude that the 2D GUA phase preferentially crystalizes at the perovskite/CTL interface, while the 2D BA phase is most likely embedded in the bulk.[48]

To investigate preferential crystallization, we turn our focus to GUA films, with two GUA concentrations ($GUA_{0.05}$ for 5 mol % GUA and $GUA_{0.1}$ for 10 mol % GUA). **Figure 2**A shows similar differential spectra for both GUA concentrations when probed from the glass side. However, when light is incident from the perovskite film side, only the $GUA_{0.1}$ film shows a significant drop in the differential absorption spectrum (Figure 2B). We then used angle-dependent grazing-incidence wide-angle X-ray scattering (GIWAXS) to acquire structural information regarding the location of 2D GUA. At an incidence angle of 0.3°, the X-ray detection depth reaches the bottom surface, confirmed by the appearance of the 2.16 A^{-1} ITO peak (Figure 2C,E), which is absent in the surface-sensitive GIWAXS pattern with a 0.1° incident angle (Figure 2D,F). In addition to the ITO peak, we observe scattering from 2D GUA at 0.83 and 0.93 A^{-1} for both $GUA_{0.05}$ and $GUA_{0.1}$ films in the 0.3° images. In contrast, the GUA_2PbI_4 peak in the $GUA_{0.05}$ film is barely visible in the 0.1° scattering pattern. These findings suggest that the 2D GUA phase does precipitate on both interfaces, but only becomes apparent on the top surface at higher GUA concentrations.[54]

Perovskite film formation has previously been seen to depend on the interplay between the perovskite precursors and the underlying substrate.[31,43,54–56] Here we reasoned that the interaction between perovskite constituents and NiO_x could play an important role in inducing preferential crystallization of 2D GUA at the buried interface. As the treated samples and control samples only differ in their organic cations, their binding with NiO_x is key to understanding the crystallization process. The

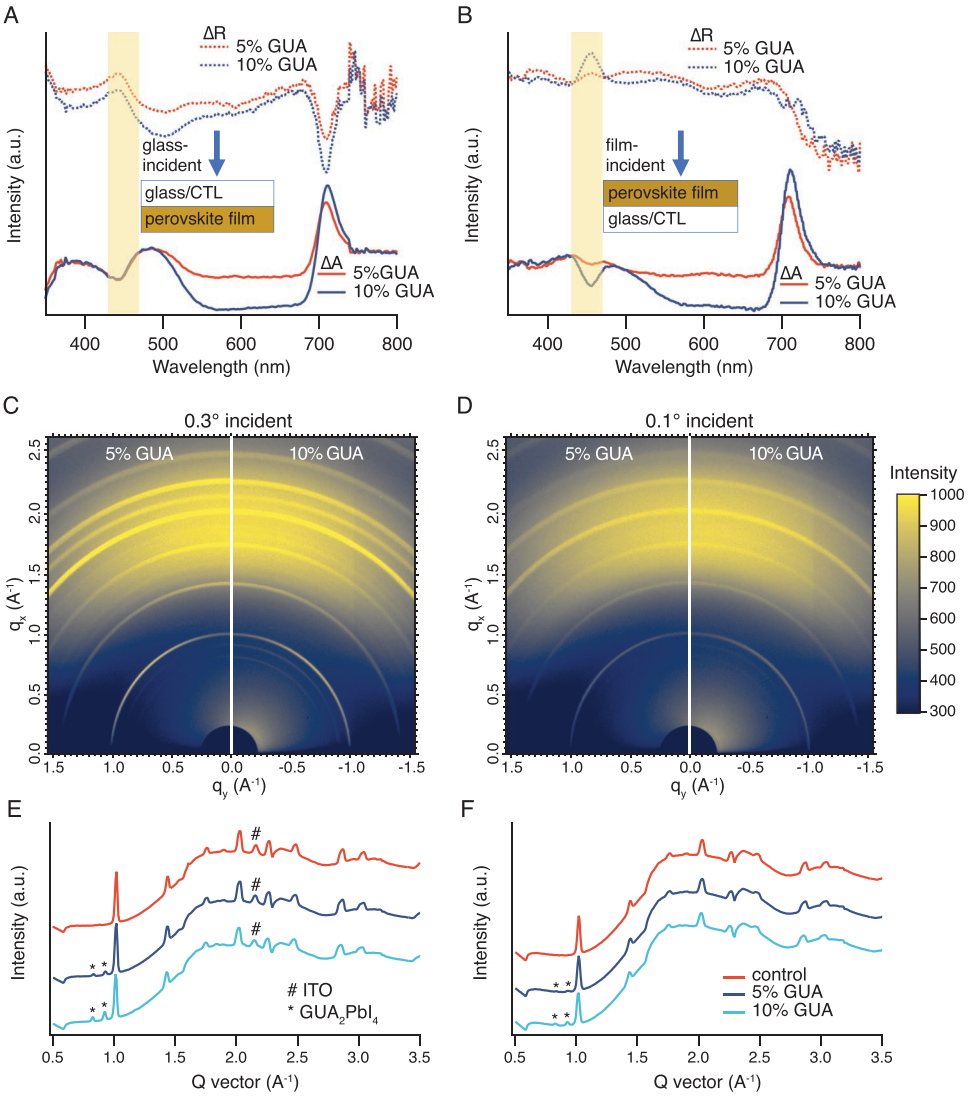

Figure 2. Preferential crystallization of 2D GUA_2PbI_4 at the perovskite/CTL interface. A) Glass-incident and B) film-incident differential absorptance and reflectance spectra of GUA films deposited on NiO_x/glass substrate. GIWAXS patterns and their circular average curves of GUA films deposited on NiO_x/ITO substrate with X-ray incident angle of C,E) 0.3° and D,F) 0.1°.

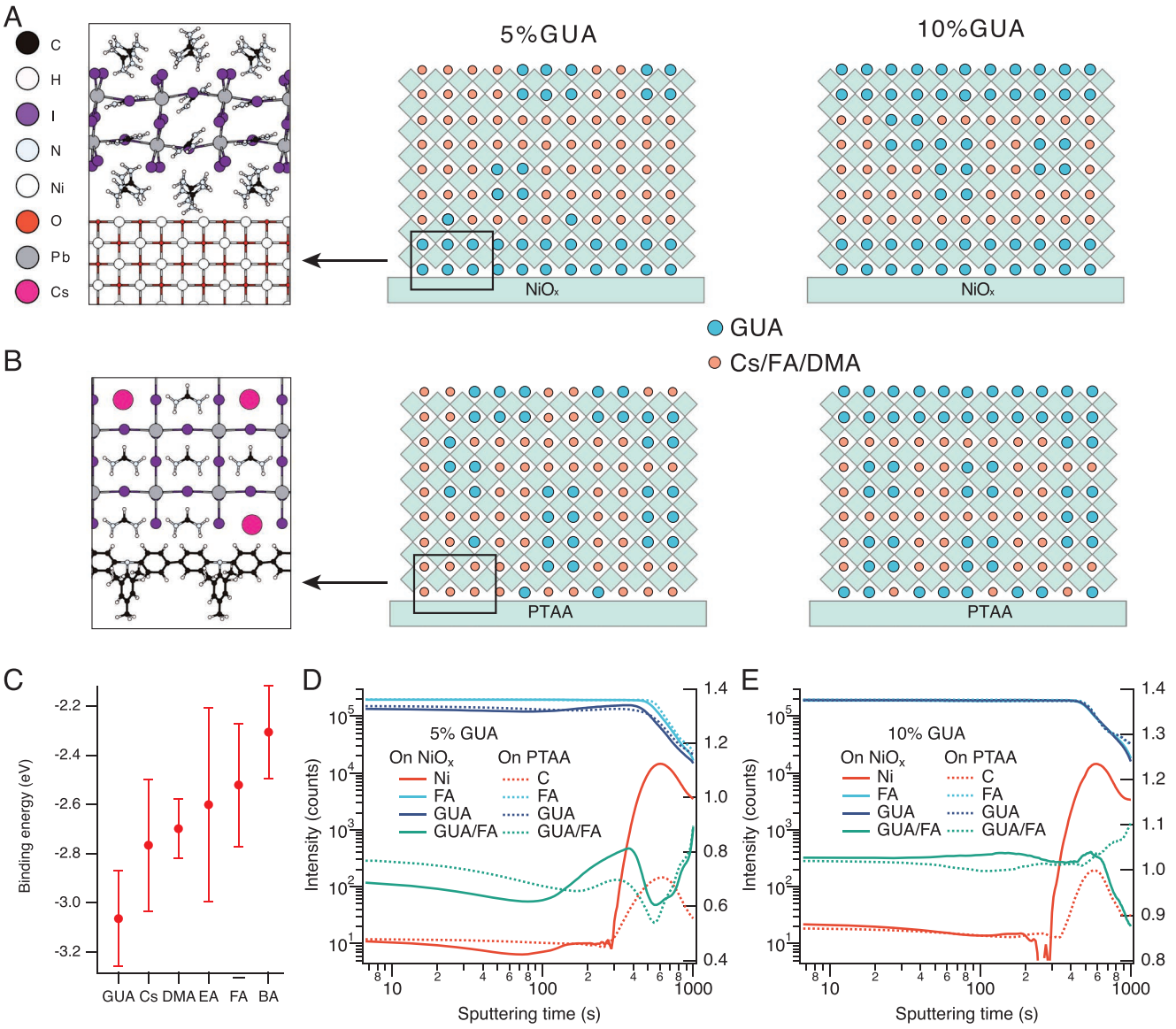

Figure 3. Mechanism of substrate-induced preferential crystallization of GUA_2PbI_4. A,B) Structural model and corresponding schematics of crystallization process for films with different GUA concentrations on NiO_x (A) and PTAA (B) substrate. C) The average binding energy of different cations with NiO_x (100), (110), and (111) surface by DFT (error bars represent standard deviations of average binding energies of different facets). D,E) TOF-SIMS depth profiling of 5% GUA (D) and 10% GUA (E) films deposited on NiO_x and PTAA substrates. GUA/FA ratios are plotted to the right axis.

highly symmetric structure of GUA and its $-NH_2$ functional groups allow it to readily form hydrogen bonds with oxygen in the NiO_x lattice. We illustrate this process in **Figure 3**A. For the $GUA_{0.05}$ composition, GUA molecules precipitate on the NiO_x surface and therefore form a GUA-rich region. These anchored GUA molecules subsequently crystalize into a thin GUA_2PbI_4 layer on the substrate during annealing. When the exposed preferential oxygen binding sites are saturated, excess GUA molecules randomly distribute throughout film, especially at higher GUA concentration ($GUA_{0.1}$). They may attach to the grain boundaries of 3D phase to produce 2D/3D structures[57] or incorporate into perovskite lattice to form mixed-cation perovskite alloy.[58,59]

We calculated, using density functional theory (DFT), the binding energy of each A-site cation in this study with the three major facets of our NiO_x nanoparticles (Figure S2, Supporting Information). GUA has the largest average binding energy with NiO_x surfaces, owing to its readily available $-NH_2$ for hydrogen bonding (Figure 3C). DMA has a lower average binding energy with NiO_x, despite more H atoms in its structure. We note that the H atoms in the DMA molecule are less prone to bond with oxygen, as C—H bonds have a less polar character than the N—H bonds in GUA. In addition, rather than bonding C—H to oxygen sites, the DMA tends to turn C—H bonds away from the NiO_x surface, exposing its only $-NH_2$ functional group to the substrate (Figure S3, Supporting Information). It is therefore a kinetically slower process and the more symmetric structure of GUA facilitates its precipitation onto the NiO_x surface.

To test this hypothesis, we spin-coated perovskite films onto a poly[bis(4-phenyl)(2,4,6-trimethylphenyl)amine (PTAA)

substrate. Its inert and hydrophobic surface minimizes the interaction with perovskite precursors.[60] GUA molecules in this case are unlikely to preferentially accumulate on the PTAA surface, and therefore are expected to mix within the bulk perovskite (Figure 3B), as evidenced by the time-of-flight secondary ion mass spectrometry (TOF-SIMS) depth profiling discussed in the next section. In addition, these GUA molecules exist, at least in part, as GUA_2PbI_4 as confirmed by XRD (Figure S4, Supporting Information). Glass-incident differential absorptance (reflectance) spectra show no drop (increase) in absorption (reflection) at ≈455 nm, indicating no preferential growth of a 2D GUA phase at the PTAA/perovskite interface (Figure S5A, Supporting Information). However, the differential optical spectra generated using the film-incident geometry show similar behavior to films deposited on the NiO_x substrate, suggesting that the 2D GUA phase still precipitates at the top surface at higher GUA concentrations (Figure S5B, Supporting Information).

Each ionic species in this study has a unique mass to charge ratio and therefore can be explicitly identified in ToF-SIMS. We obtained chemical profiles as a function of position throughout the film thickness (Figure 3D,E). The rise in intensity of Ni or C signals the emergence of the buried interface of films deposited on NiO_x and PTAA.[61] While FA profiles are independent of substrate type, vertical distributions of guanidinium exhibit a stark difference in $GUA_{0.05}$ films grown on these two substrates. Specifically, GUA concentration increases sharply by 15% at the bottom surface on NiO_x, but decreases steadily by 13% on PTAA (Figure 3D). The distribution of cations in $GUA_{0.1}$ films is less affected by the choice of substrate: we observed a flattening of GUA profile on both substrates, suggesting the mixing of 2D/3D structure,[57] or cation alloying[62] within the bulk (Figure 3E). We note that the PL of treated films is slightly red-shifted than the control (**Figure 4**B), which is consistent with the GUA alloying interpretation.[63] Nonetheless, the NiO_x interface still has a greater GUA concentration than the PTAA interface, in agreement with the preferential adsorption model. These findings are also supported by depth-dependent X-ray photoelectron spectroscopy spectra (Figure S6, Supporting Information).

We used time-resolved photoluminescence (TRPL) spectroscopy to explore the effect of the GUA_2PbI_4 layer on carrier recombination dynamics at the NiO_x/perovskite interface. We note that PL decays of perovskite films on a charge transport layer are affected by two processes—charge extraction and increased non-radiative recombination losses. We fitted decay curves by biexponential functions to obtain two decay components. As pointed out previously,[10] the fast decay is due to carrier extraction into the transport layer, and the slow decay represents bulk lifetime subjected to additional non-radiative interface recombination.[10] Therefore, we refer to the slower time components as the lifetimes that our discussion is based on. With proper top surface passivation by trioctylphosphine oxide (TOPO), carrier lifetimes are only limited by non-radiative recombination at the bottom interface[63] (Figure S7, Supporting Information). Lifetimes of perovskites deposited on NiO_x are 10–20 times shorter than they are on glass (Table S1, Supporting Information), confirming a significant contribution of NiO_x/perovskite interface to non-radiative recombination. In this case, both $GUA_{0.05}$ and $GUA_{0.1}$ film on NiO_x have more than doubled lifetime than the control sample (Figure 4A), signifying the passivation effect of 2D GUA.

TRPL results are corroborated with steady-state PL measurement at open circuit, during which the quasi-Fermi level splitting is maintained throughout the experiment and the quenching due to charge extraction is negligible.[64] Therefore, the greater quenched steady PL intensity of control film when it is in contact with NiO_x is due to the more severe interface non-radiative recombination, compared to GUA samples (Figure 4B). We further calculated the SRV of the NiO_x/perovskite interface by fitting PL lifetimes as a function of film thickness[63] (Figure 4C). SRV decreases by ≈4 × from 411 ± 56 to 114 ± 10 cm s^{-1} at the $NiO_x/GUA_{0.05}$ interface, indicating passivation by the GUA_2PbI_4 at the buried interface. We note that bulk passivation (e.g., by 2D/3D structure within bulk perovskite films[57]) is also at play, but the effect is minor (12% longer bulk lifetime) compared to the interface passivation (72% reduction in SRV).

The passivation of the perovskite/CTL interface using spontaneously formed GUA_2PbI_4 leads to an increased V_{oc} of 65 meV (**Table 1**) for inverted structure solar cells using a NiO_x

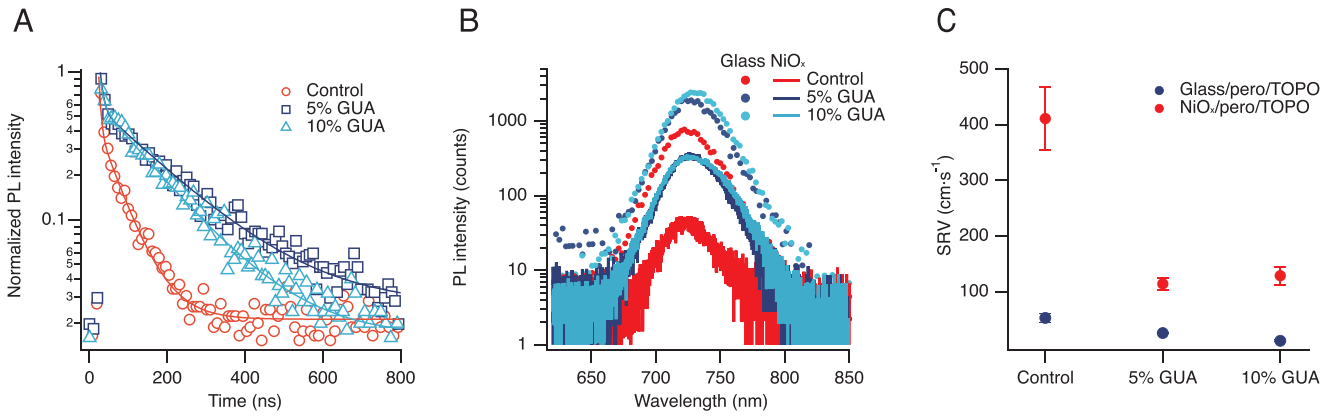

Figure 4. Passivation effect of GUA_2PbI_4 layer. A) TRPL decays of TOPO-passivated films deposited on NiO_x. B) Steady-state PL spectra of TOPO-passivated films deposited on glass and NiO_x substrates. C) Extracted SRV of films deposited on glass and NiO_x substrates.

Table 1. Statistics of 1.7 eV device performance.

	PCE [%]	V_{oc} [mV]	J_{sc} [mA·cm^{-2}]	FF [%]	HI[a)] [%]
Control	18.1 ± 0.5	1155 ± 8	19.9 ± 0.5	78.9 ± 1.4	1.2 ± 1.2
Champion	18.7	1149	20.2	80.5	0.8
3% GUA	18.3 ± 0.3	1171 ± 12	20.0 ± 0.2	78.1 ± 1.2	0.8 ± 0.9
Champion	18.5	1176	20.1	78.3	0.4
5% GUA	19.8 ± 0.2	1220 ± 5	19.7 ± 0.3	82.6 ± 1.5	0.2 ± 0.4
Champion	20.1	1226	20.1	81.6	0.5
7% GUA	18.3 ± 0.7	1209 ± 7	19.0 ± 0.5	79.7 ± 2.4	0.9 ± 0.6
Champion	19.2	1213	19.2	82.2	0.6
10% GUA	17.6 ± 0.3	1197 ± 9	18.7 ± 0.1	77.7 ± 2.9	0.6 ± 0.6
Champion	18.1	1199	18.8	80.4	2.7

[a)]Hysteresis index (HI) = $\left|\frac{PCE_{RS} - PCE_{FS}}{PCE_{RS}}\right|$.

HTL. **Figure 5**B shows an external quantum efficiency (EQE) drop at ≈455 nm with increasing GUA concentration, a result of reduced absorption in the bulk film (Figure S8, Supporting Information) due in part to reflection and primarily parasitic absorption of the GUA_2PbI_4 phase. High GUA concentration leads to reduced J_{sc} and FF as a result of the parasitic absorption and the insulating nature of wide bandgap 2D layers. 5% GUA balances V_{oc} and J_{sc} and results in a champion PCE of 20.1% and a stabilized power output of 19.6% (Figure 5A). The 1.23 V V_{oc} is the highest among devices using NiO_x as HTL (Table S2, Supporting Information). We evaluated the stability of unencapsulated devices using room temperature 1-sun maximum power point (MPP) tracking and shelf lifetime testing. Device stability increases with 5% GUA concentration (Figure 5C), benefiting from the stable 2D/3D structure.[31] We note that PCE deteriorates faster with higher GUA concentration, possibly due to the gradual formation of less stable, higher n-value 2D species.[65,66]

To investigate the general nature of this spontaneous passivation strategy, we further compared two variations: a different perovskite composition – 1.55 eV bandgap in p–i–n structure (Figure S9, Supporting Information) and a different device structure – 1.7 eV bandgap in n–i–p structure using SnO_2 substrate (Figure S10, Supporting Information). Films with GUA exhibited improved V_{oc} and similar dips in their EQE spectra at ≈455 nm in both cases, implying the formation of 2D GUA perovskite at the buried interface. An average increase in V_{oc} of 100 mV in resultant n–i–p devices and a champion PCE of 22.9% for p–i–n devices indicate the wider applicability of this passivation strategy.

3. Conclusions

This work demonstrates a facile method to produce effective 2D perovskite passivation at the buried perovskite/CTL interface. We show that large organic cations can be used to spontaneously form a 2D buffer layer at the buried interface. The crystallization dynamics are highly dependent on the interaction between the surface chemistry of the CTL substrate and the components in the perovskite precursor. Strong binding of cations to the substrate induces a preferential crystallization of the 2D perovskite phase, which can function as a passivating layer, leading to higher V_{oc} in the resulting solar cells. We note that previous reports of improved V_{oc} using GUA as additives may have taken the focus off of the interface passivation

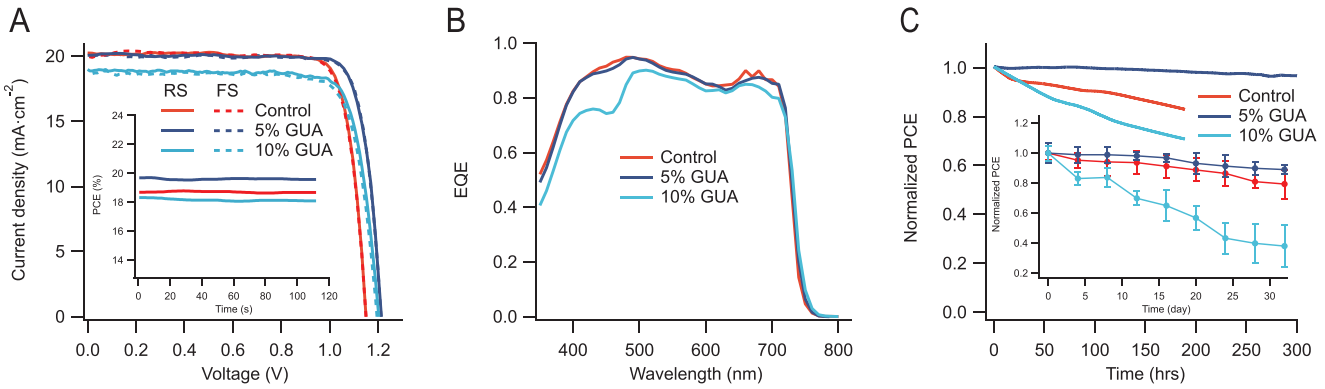

Figure 5. Photovoltaic device performance of different perovskites. A) Current density–voltage curves (solid line: reverse scan; dash line: forward scan) and B) EQE spectra of perovskite devices containing 0, 5, and 10% GUA. C) MPP stability tracking of unencapsulated devices under 1-sun condition in N_2-filled environment. Inset shows shelf lifetimes of devices stored in the dark glovebox.

effect, concentrating instead on bulk effects such as cation alloying[58,62] and grain boundary passivation.[57]

This represents a promising new route towards improving device performance for PSCs using metal oxide CTLs, as we expect other metal-oxide/2D-cation combinations to produce similar results. The design of perovskite/CTL interfaces that provide effective binding sites for passivating 2D cations is worthy of further exploration. At the same time, one needs to balance the competing effect of surface passivation (improving V_{oc}) and the parasitic absorption of the 2D phase (reducing J_{sc}) to achieve the optimized PCE.

As PCEs move closer towards theoretical limits, passivation of the buried interface is likely to become more pertinent. This work provides valuable insight into the mechanism of buried interface passivation and will assist with future development of PSCs by dual-interface engineering.

Supporting Information

Supporting Information is available from the Wiley Online Library or from the author.

Acknowledgements

B.C. and H.C. contributed equally to this work. This research was made possible by Ontario Research Fund-Research Excellence program (ORF7-Ministry of Research and Innovation, Ontario Research Fund-Research Excellence Round 7). This work was also supported by the U.S. Department of the Navy, Office of Naval Research (N00014-17-1-2524 and N00014-20-1-2572).

Conflict of Interest

The authors declare no conflict of interest.

Data Availability Statement

The data that support the findings of this study are available from the corresponding author upon reasonable request.

Keywords

interface passivation, perovskites, solar cells

Received: May 4, 2021
Revised: July 5, 2021
Published online:

[1] W. A. Dunlap-Shohl, Y. Zhou, N. P. Padture, D. B. Mitzi, *Chem. Rev.* **2019**, *119*, 3193.
[2] Best Research-Cell Efficiency Chart | Photovoltaic Research | NREL https://www.nrel.gov/pv/cell-efficiency.html (accessed: August 2019).
[3] Q. Jiang, Y. Zhao, X. Zhang, X. Yang, Y. Chen, Z. Chu, Q. Ye, X. Li, Z. Yin, J. You, *Nat. Photonics* **2019**, *13*, 460.
[4] M. Stolterfoht, P. Caprioglio, C. M. Wolff, J. A. Márquez, J. Nordmann, S. Zhang, D. Rothhardt, U. Hörmann, Y. Amir, A. Redinger, L. Kegelmann, F. Zu, S. Albrecht, N. Koch, T. Kirchartz, M. Saliba, T. Unold, D. Neher, *Energy Environ. Sci.* **2019**, *12*, 2778.
[5] C. Ma, N.-G. Park, *Chem* **2020**, *6*, 1254.
[6] Y. Hou, E. Aydin, M. De Bastiani, C. Xiao, F. H. Isikgor, D.-J. Xue, B. Chen, H. Chen, B. Bahrami, A. H. Chowdhury, A. Johnston, S.-W. Baek, Z. Huang, M. Wei, Y. Dong, J. Troughton, R. Jalmood, A. J. Mirabelli, T. G. Allen, E. Van Kerschaver, M. I. Saidaminov, D. Baran, Q. Qiao, K. Zhu, S. De Wolf, E. H. Sargent, *Science* **2020**, *367*, 1135.
[7] T. Leijtens, K. A. Bush, R. Prasanna, M. D. McGehee, *Nat. Energy* **2018**, *3*, 828.
[8] S. Mahesh, J. M. Ball, R. D. J. Oliver, D. P. McMeekin, P. K. Nayak, M. B. Johnston, H. J. Snaith, *Energy Environ. Sci.* **2020**, *13*, 258.
[9] S. D. Stranks, G. E. Eperon, G. Grancini, C. Menelaou, M. J. P. Alcocer, T. Leijtens, L. M. Herz, A. Petrozza, H. J. Snaith, *Science* **2013**, *342*, 341.
[10] M. Stolterfoht, C. M. Wolff, J. A. Márquez, S. Zhang, C. J. Hages, D. Rothhardt, S. Albrecht, P. L. Burn, P. Meredith, T. Unold, D. Neher, *Nat. Energy* **2018**, *3*, 847.
[11] Z. Ni, C. Bao, Y. Liu, Q. Jiang, W.-Q. Wu, S. Chen, X. Dai, B. Chen, B. Hartweg, Z. Yu, Z. Holman, J. Huang, *Science* **2020**, *367*, 1352.
[12] X. Yin, Y. Guo, H. Xie, W. Que, L. B. Kong, *Sol. RRL* **2019**, *3*, 1900001.
[13] H. Chen, Q. Wei, M. I. Saidaminov, F. Wang, A. Johnston, Y. Hou, Z. Peng, K. Xu, W. Zhou, Z. Liu, L. Qiao, X. Wang, S. Xu, J. Li, R. Long, Y. Ke, E. H. Sargent, Z. Ning, *Adv. Mater.* **2019**, *31*, 1903559.
[14] X. Zheng, Y. Hou, C. Bao, J. Yin, F. Yuan, Z. Huang, K. Song, J. Liu, J. Troughton, N. Gasparini, C. Zhou, Y. Lin, D.-J. Xue, B. Chen, A. K. Johnston, N. Wei, M. N. Hedhili, M. Wei, A. Y. Alsalloum, P. Maity, B. Turedi, C. Yang, D. Baran, T. D. Anthopoulos, Y. Han, Z.-H. Lu, O. F. Mohammed, F. Gao, E. H. Sargent, O. M. Bakr, *Nat. Energy* **2020**, *5*, 131.
[15] C. J. Flynn, S. M. McCullough, E. Oh, L. Li, C. C. Mercado, B. H. Farnum, W. Li, C. L. Donley, W. You, A. J. Nozik, J. R. McBride, T. J. Meyer, Y. Kanai, J. F. Cahoon, *ACS Appl. Mater. Interfaces* **2016**, *8*, 4754.
[16] E. H. Jung, B. Chen, K. Bertens, M. Vafaie, S. Teale, A. Proppe, Y. Hou, T. Zhu, C. Zheng, E. H. Sargent, *ACS Energy Lett.* **2020**, *5*, 2796.
[17] W. Chen, Y. Zhou, G. Chen, Y. Wu, B. Tu, F. Liu, L. Huang, A. M. C. Ng, A. B. Djurišić, Z. He, *Adv. Energy Mater.* **2019**, *9*, 1803872.
[18] C. C. Boyd, R. C. Shallcross, T. Moot, R. Kerner, L. Bertoluzzi, A. Onno, S. Kavadiya, C. Chosy, E. J. Wolf, J. Werner, J. A. Raiford, C. de Paula, A. F. Palmstrom, Z. J. Yu, J. J. Berry, S. F. Bent, Z. C. Holman, J. M. Luther, E. L. Ratcliff, N. R. Armstrong, M. D. McGehee, *Joule* **2020**, *4*, 1759.
[19] S. Teale, A. H. Proppe, E. H. Jung, A. Johnston, D. H. Parmar, B. Chen, Y. Hou, S. O. Kelley, E. H. Sargent, *J. Phys. Chem. Lett.* **2020**, *11*, 5115.
[20] E. A. Alharbi, A. Y. Alyamani, D. J. Kubicki, A. R. Uhl, B. J. Walder, A. Q. Alanazi, J. Luo, A. Burgos-Caminal, A. Albadri, H. Albrithen, M. H. Alotaibi, J.-E. Moser, S. M. Zakeeruddin, F. Giordano, L. Emsley, M. Grätzel, *Nat. Commun.* **2019**, *10*, 3008.
[21] Y. Shao, Z. Xiao, C. Bi, Y. Yuan, J. Huang, *Nat. Commun.* **2014**, *5*, 5784.
[22] A. Abate, M. Saliba, D. J. Hollman, S. D. Stranks, K. Wojciechowski, R. Avolio, G. Grancini, A. Petrozza, H. J. Snaith, *Nano Lett.* **2014**, *14*, 3247.
[23] R. Wang, J. Xue, K.-L. Wang, Z.-K. Wang, Y. Luo, D. Fenning, G. Xu, S. Nuryyeva, T. Huang, Y. Zhao, J. L. Yang, J. Zhu, M. Wang, S. Tan, I. Yavuz, K. N. Houk, Y. Yang, *Science* **2019**, *366*, 1509.
[24] M. A. Mahmud, T. Duong, Y. Yin, H. T. Pham, D. Walter, J. Peng, Y. Wu, L. Li, H. Shen, N. Wu, N. Mozaffari, G. Andersson,

K. R. Catchpole, K. J. Weber, T. P. White, *Adv. Funct. Mater.* **2020**, *30*, 1907962.
[25] X. Zheng, B. Chen, J. Dai, Y. Fang, Y. Bai, Y. Lin, H. Wei, X. C. Zeng, J. Huang, *Nat. Energy* **2017**, *2*, 17102.
[26] M. Jaysankar, B. A. L. Raul, J. Bastos, C. Burgess, C. Weijtens, M. Creatore, T. Aernouts, Y. Kuang, R. Gehlhaar, A. Hadipour, J. Poortmans, *ACS Energy Lett.* **2019**, *4*, 259.
[27] S. Yang, S. Chen, E. Mosconi, Y. Fang, X. Xiao, C. Wang, Y. Zhou, Z. Yu, J. Zhao, Y. Gao, F. De Angelis, J. Huang, *Science* **2019**, *365*, 473.
[28] R. D. Chavan, D. Prochowicz, M. M. Tavakoli, P. Yadav, C. K. Hong, *Adv. Mater. Interfaces* **2020**, *7*, 2000105.
[29] Y. Zheng, X. Yang, R. Su, P. Wu, Q. Gong, R. Zhu, *Adv. Funct. Mater.* **2020**, *30*, 2000457.
[30] S. Gharibzadeh, B. Abdollahi Nejand, M. Jakoby, T. Abzieher, D. Hauschild, S. Moghadamzadeh, J. A. Schwenzer, P. Brenner, R. Schmager, A. A. Haghighirad, L. Weinhardt, U. Lemmer, B. S. Richards, I. A. Howard, U. W. Paetzold, *Adv. Energy Mater.* **2019**, *9*, 1803699.
[31] G. Grancini, C. Roldán-Carmona, I. Zimmermann, E. Mosconi, X. Lee, D. Martineau, S. Narbey, F. Oswald, F. De Angelis, M. Graetzel, M. K. Nazeeruddin, *Nat. Commun.* **2017**, *8*, 15684.
[32] J. Chen, J.-Y. Seo, N.-G. Park, *Adv. Energy Mater.* **2018**, *8*, 1702714.
[33] P. Chen, Y. Bai, S. Wang, M. Lyu, J.-H. Yun, L. Wang, *Adv. Funct. Mater.* **2018**, *28*, 1706923.
[34] A. H. Proppe, M. Wei, B. Chen, R. Quintero-Bermudez, S. O. Kelley, E. H. Sargent, *J. Am. Chem. Soc.* **2019**, *141*, 14180.
[35] A. Agresti, S. Pescetelli, A. L. Palma, A. E. Del Rio, D. Castillo, G. Konios, S. Kakavelakis, L. Razza, E. Cinà, F. Kymakis, A. Bonaccorso, C. Di, *ACS Energy Lett.* **2017**, *2*, 279.
[36] A. Agresti, S. Pescetelli, A. L. Palma, B. Martín-García, L. Najafi, S. Bellani, I. Moreels, M. Prato, F. Bonaccorso, A. Di, Carlo, *ACS Energy Lett.* **2019**, *4*, 1862.
[37] J. Li, M. Wu, G. Yang, D. Zhang, Z. Wang, D. Zheng, J. Yu, *Sol. Energy* **2020**, *205*, 44.
[38] F. Zhang, C. Xiao, X. Chen, B. W. Larson, S. P. Harvey, J. J. Berry, K. Zhu, *Joule* **2019**, *3*, 1452.
[39] L. Najafi, B. Taheri, B. Martín-García, S. Bellani, D. Di Girolamo, A. Agresti, R. Oropesa-Nuñez, S. Pescetelli, L. Vesce, E. Calabrò, M. Prato, A. E. Del Rio Castillo, A. Di Carlo, F. Bonaccorso, *ACS Nano* **2018**, *12*, 10736.
[40] M. M. Tavakoli, P. Yadav, R. Tavakoli, J. Kong, *Adv. Energy Mater.* **2018**, *8*, 1800794.
[41] J. Peng, Y. Wu, W. Ye, D. A. Jacobs, H. Shen, X. Fu, Y. Wan, T. Duong, N. Wu, C. Barugkin, H. T. Nguyen, D. Zhong, J. Li, T. Lu, Y. Liu, M. N. Lockrey, K. J. Weber, K. R. Catchpole, T. P. White, *Energy Environ. Sci.* **2017**, *10*, 1792.
[42] J. Peng, J. I. Khan, W. Liu, E. Ugur, T. Duong, Y. Wu, H. Shen, K. Wang, H. Dang, E. Aydin, X. Yang, Y. Wan, K. J. Weber, K. R. Catchpole, F. Laquai, S. De Wolf, T. P. White, *Adv. Energy Mater.* **2018**, *8*, 1801208.
[43] Y. Cheng, M. Li, X. Liu, S. H. Cheung, H. T. Chandran, H.-W. Li, X. Xu, Y.-M. Xie, S. K. So, H.-L. Yip, S.-W. Tsang, *Nano Energy* **2019**, *61*, 496.
[44] Y. Zhao, Q. Li, W. Zhou, Y. Hou, Y. Zhao, R. Fu, D. Yu, X. Liu, Q. Zhao, *Sol. RRL* **2018**, *3*, 1800296.
[45] G. Tumen-Ulzii, C. Qin, D. Klotz, M. R. Leyden, P. Wang, M. Auffray, T. Fujihara, T. Matsushima, J.-W. Lee, S.-J. Lee, Y. Yang, C. Adachi, *Adv. Mater.* **2020**, *32*, 1905035.
[46] A. F. Palmstrom, G. E. Eperon, T. Leijtens, R. Prasanna, S. N. Habisreutinger, W. Nemeth, E. A. Gaulding, S. P. Dunfield, M. Reese, S. Nanayakkara, T. Moot, J. Werner, J. Liu, B. To, S. T. Christensen, M. D. McGehee, M. F. A. M. van Hest, J. M. Luther, J. J. Berry, D. T. Moore, *Joule* **2019**, *3*, 2193.
[47] C. C. Stoumpos, D. H. Cao, D. J. Clark, J. Young, J. M. Rondinelli, J. I. Jang, J. T. Hupp, M. G. Kanatzidis, *Chem. Mater.* **2016**, *28*, 2852.
[48] Z. Wang, Q. Lin, F. P. Chmiel, N. Sakai, L. M. Herz, H. J. Snaith, *Nat. Energy* **2017**, *2*, 17135.
[49] M. Szafrański, A. Katrusiak, *Phys. Rev. B: Condens. Matter Mater. Phys.* **2000**, *61*, 1026.
[50] Z. Deng, G. Kieslich, P. D. Bristowe, A. K. Cheetham, S. Sun, *APL Mater.* **2018**, *6*, 114202.
[51] A. M. Fox, *Department of Physics and Astronomy Mark Fox, Optical Properties of Solids*, Oxford University Press, Oxford, UK **2001**.
[52] J. Li, J. Wang, J. Ma, H. Shen, L. Li, X. Duan, D. Li, *Nat. Commun.* **2019**, *10*, 806.
[53] B. Liu, C. M. M. Soe, C. C. Stoumpos, W. Nie, H. Tsai, K. Lim, A. D. Mohite, M. G. Kanatzidis, T. J. Marks, K. D. Singer, *Sol. RRL* **2017**, *1*, 1700062.
[54] E. Climent-Pascual, B. C. Hames, J. S. Moreno-Ramírez, A. L. Álvarez, E. J. Juarez-Perez, E. Mas-Marza, I. Mora-Seró, A. de Andrés, C. Coya, *J. Mater. Chem. A* **2016**, *4*, 18153.
[55] S. Olthof, K. Meerholz, *Sci. Rep.* **2017**, *7*, 40267.
[56] B. Zhao, Y. Lian, L. Cui, G. Divitini, G. Kusch, E. Ruggeri, F. Auras, W. Li, D. Yang, B. Zhu, R. A. Oliver, J. L. MacManus-Driscoll, S. D. Stranks, D. Di, R. H. Friend, *Nat. Electron.* **2020**, *3*, 704.
[57] J. Tong, Z. Song, D. H. Kim, X. Chen, C. Chen, A. F. Palmstrom, P. F. Ndione, M. O. Reese, S. P. Dunfield, O. G. Reid, J. Liu, F. Zhang, S. P. Harvey, Z. Li, S. T. Christensen, G. Teeter, D. Zhao, M. M. Al-Jassim, M. F. A. M. van Hest, M. C. Beard, S. E. Shaheen, J. J. Berry, Y. Yan, K. Zhu, *Science* **2019**, *364*, 475.
[58] A. D. Jodlowski, C. Roldán-Carmona, G. Grancini, M. Salado, M. Ralaiarisoa, S. Ahmad, N. Koch, L. Camacho, G. de Miguel, M. K. Nazeeruddin, *Nat. Energy* **2017**, *2*, 972.
[59] E. Vega, M. Mollar, B. Marí, *J. Alloys Compd.* **2018**, *739*, 1059.
[60] C. Bi, Q. Wang, Y. Shao, Y. Yuan, Z. Xiao, J. Huang, *Nat. Commun.* **2015**, *6*, 7747.
[61] F. Fu, S. Pisoni, Q. Jeangros, J. Sastre-Pellicer, M. Kawecki, A. Paracchino, T. Moser, J. Werner, C. Andres, L. Duchêne, P. Fiala, M. Rawlence, S. Nicolay, C. Ballif, A. N. Tiwari, S. Buecheler, *Energy Environ. Sci.* **2019**, *12*, 3074.
[62] R. J. Stoddard, A. Rajagopal, R. L. Palmer, I. L. Braly, A. K.-Y. Jen, H. W. Hillhouse, *ACS Energy Lett.* **2018**, *3*, 1261.
[63] J. Wang, W. Fu, S. Jariwala, I. Sinha, A. K.-Y. Jen, D. S. Ginger, *ACS Energy Lett.* **2019**, *4*, 222.
[64] T. Kirchartz, J. A. Márquez, M. Stolterfoht, T. Unold, *Adv. Energy Mater.* **2020**, *10*, 1904134.
[65] A. A. Sutanto, N. Drigo, V. I. E. Queloz, I. Garcia-Benito, A. R. Kirmani, L. J. Richter, P. A. Schouwink, K. T. Cho, S. Paek, M. K. Nazeeruddin, G. Grancini, *J. Mater. Chem. A* **2020**, *8*, 2343.
[66] L. N. Quan, M. Yuan, R. Comin, O. Voznyy, E. M. Beauregard, S. Hoogland, A. Buin, A. R. Kirmani, K. Zhao, A. Amassian, D. H. Kim, E. H. Sargent, *J. Am. Chem. Soc.* **2016**, *138*, 2649.